KRONOS FUSION ENERGY

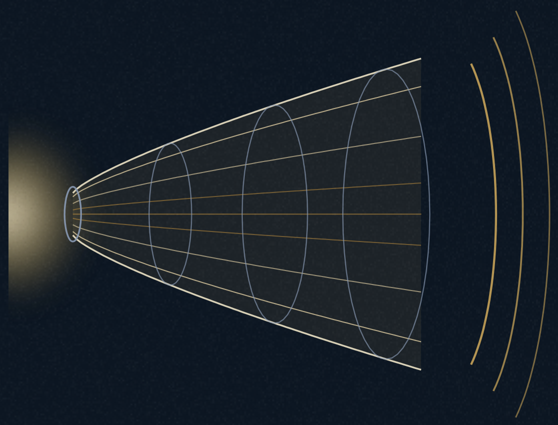

PAPER 2.64 · THE KRONOS 2026 SERIES

Direct-Energy-Converter Architectures for a D–^{3}He Tandem-Mirror Burner: Venetian-Blind, Traveling-Wave, and Periodic-Electrostatic-Plug Collectors Compared on Efficiency, Grid Erosion, and Lifetime

A deuterium–helium-3 tandem-mirror burner deposits most of its fusion power in charged particles that leave the machine axially as a fast, directed ion stream, so the...

Read it live — 3-D model · physics validator · film series

BY P I FORD AND G L KULCINSKI

2026 · EDITORIAL EDITION

THE OFFICIAL RECORD

What this document is, and how to read its numbers

This is a combined editorial. It gathers, in one volume, the two design studies Kronos Fusion Energy released in 2026 — a compact spherical-tokamak tritium/helium-3 breeder and a deuterium–helium-3 tandem-mirror generator — together with the intellectual-property estate, the people, and, in the internal edition, the full commercial case. The scientific text is the same text that appears in the arXiv preprints and the journal submissions; the editorial adds the apparatus a reader needs to hold the whole program at once, and nothing in the physics is altered to fit it.

THE HONESTY STANCE IS THE ASSET

Every headline quantity carries an **evidence class** — DERIVED RECOMPUTED MEASURED REQUIREMENT — and, where a number is a modelled extrapolation rather than a demonstrated value, it is labelled as such and its downside is shown next to it. Several quantities in the underlying corpus moved after first publication; where a value has been withdrawn or restated, the record says so plainly. This is deliberate: a diligence team will find the load-bearing assumptions, so the document surfaces them first.

TWO EDITIONS

This volume is issued in two editions. The **public edition** (light) carries the physics and the design only — no dollar, price, or per-kilogram figure appears anywhere in it. The **internal edition** (dark) adds the economics, the funding architecture, and the defense-commercial analysis, and is marked *Confidential* accordingly; it is not for public distribution. Where the commercial case rests on a modelled assumption rather than a demonstrated one, it is labelled as such and its downside is shown alongside it, on the same terms as the physics.

TITLE	The Kronos Fleet — Hyperion · Aegis · MetroVolt: A Combined Design & Commercialization Study
AUTHOR	Priyanca Ford, Founder & CEO, on behalf of Kronos Fusion Energy
EDITION	2026 Combined Editorial · first issue
COMPANION WORKS	The five-paper arXiv drop — (1) Breeder, (2) Burner, (3) REBCO magnet & tape, (4) Direct Energy Conversion, (5) AI/ML/Quantum control — with matching numbered Zenodo deposits, plus the IOP journal and IAEA-FEC submissions. Patents were filed before the drop.
NAMING	Hyperion = the breeder; Aegis (defense) and MetroVolt (data-center) = one generator in two housings. Internal mode letters (D1, L) do not appear on public surfaces.
STATUS	Conceptual design & simulation study. Nothing herein is a construction commitment.

HOW TO READ THIS VOLUME

The fleet at a glance, and the way its numbers are marked

This volume opens with *Orientation*, presents the five research papers as a bound sequence, and closes with the *Apparatus*. *Foundations* sets out the three general results both machines rest on. *Paper One* is the Hyperion breeder; *Paper Two* the Aegis / MetroVolt generator; *Papers Three, Four and Five* are the enabling science — high-field REBCO magnets and tape, direct energy conversion, and the AI / ML / quantum control stack. A *Digital Twin & 3-D Model* part follows, then the *Environmental* profile. The *Economics* and levelized cost and the *Business Case* and diligence record appear in the internal edition only; the *Simulations* proof record and the Apparatus — patent portfolio, team, limitations, and sources — close both editions.

THE FLEET AT A GLANCE

	HYPERION	AEGIS	METROVOLT
Role	Strategic-isotope foundry	Defense installation power	Campus power
Machine	**Spherical tokamak**	**Tandem mirror**	**Tandem mirror**
Fuel	Deuterium–tritium	Deuterium–helium-3	Deuterium–helium-3
Delivers	Tritium · ^{3}He · 14 MeV n	Resilient installation power	Firm campus power
Physics bar	**Fusion gain only**	Closure (gates named)	Closure + lunar ^{3}He
In the fleet	Breeds the fuel	Proves the generator	Commercial destination

HOW THE NUMBERS ARE MARKED

Every headline quantity carries an evidence class — DERIVED from first principles, RECOMPUTED from raw data, MEASURED in hardware, or a REQUIREMENT yet to be met. Financial figures carry a case label and are confined to the internal (confidential) edition. Values that moved after first publication are shown as withdrawn or restated rather than quietly changed. A capability you can evaluate is one whose limits are on the page.

ABSTRACT

Direct-Energy-Converter Architectures for a D–^{3}He Tandem-Mirror Burner: Venetian-Blind, Traveling-Wave, and Periodic-Electrostatic-Plug Collectors Compared on Efficiency, Grid Erosion, and Lifetime

A deuterium–helium-3 tandem-mirror burner deposits most of its fusion power in charged particles that leave the machine axially as a fast, directed ion stream, so the direct-energy converter (DEC) is the single component that sets the plant's electrical efficiency. The architecture that supplies the frozen module efficiency $\eta_{\mathrm{DEC}} = 0.70$ is not, however, uniquely determined by that number: three collector families—the periodic multi-stage electrostatic collector, the traveling-wave DEC (TWDEC), and the Venetian-blind collector of Moir and Barr, together with a periodic-electrostatic-plug variant—each behave very differently on the *raw* energy spread of the exhaust. We formalise the down-select. From the frozen operating point we derive the incident end-loss spectrum as a flux-weighted Maxwellian above the ion-confining potential ($\varphi_i = 248.7\,\mathrm{keV}$, $T_i = 90\,\mathrm{keV}$), giving a mean energy of $428.5\,\mathrm{keV}$, a 1st–99th-percentile band of 262–845 keV, and a raw fractional spread of $\approx 34\%$. We cast the multi-stage electrostatic collector as a retarding-field quantile-optimisation problem and prove that its module efficiency is bounded above by the grid transparency η_{grid}; solved by Monte Carlo over the full spectrum it clears 0.70 at three stages (0.727), reaches 0.834 at six, and asymptotes to $\eta_{\mathrm{grid}} = 0.93$. We model the TWDEC as a Gaussian velocity-acceptance response and show analytically that its extraction efficiency collapses as $\exp[-\sigma_E^2/(8\sigma_{\mathrm{acc}}^2)]$: it delivers 0.75–0.80 on a narrow ($< 10\%$) pre-bunched beam but only 0.51 at the raw 34% spread—below the electrostatic baseline—so it is retained as a second-stage option behind a velocity-buncher rather than the primary. Applied to the fraction $f_{\mathrm{dir}} = 0.49$ of the exhaust routed to direct conversion, the selected periodic electrostatic collector delivers the frozen burner engineering gain $Q_E = 1.318$ with headroom rather than at the edge. All results were produced on the Kronos NVIDIA GPU HPC campaign. The one open engineering item is grid erosion and lifetime under the sustained $428\,\mathrm{keV}$ end-loss flux, which sets the collector maintenance interval and does not change the architecture selection.

Open-access deposit (code & data, CC BY 4.0): DOI 10.5281/zenodo.22645935 · Zenodo community *kronos_fusion_energy*. Explore it live: interactive 3-D model · physics validator.

Keywords: direct energy conversion · traveling-wave DEC · Venetian-blind collector · tandem mirror · helium-3 burner · retarding-field collector · grid erosion

CONTENTS

Table of Contents

NOMENCLATURE

Symbols, units, and the names of things

Q	plasma (fusion) gain, P_{fus}/P_{aux}
Q_E	engineering gain, net electric out / recirculating in
H_{98}	confinement enhancement over the IPB98(y,2) scaling
Z_{eff}	effective ion charge
c_{ee}	electron–electron bremsstrahlung leading coefficient, 2.120022 (exact)
τ_E	energy confinement time
I_p	plasma current
R_0, a	major radius, minor radius
κ, δ	elongation, triangularity
β_N	normalized plasma beta (Troyon-normalized)
TBR	tritium breeding ratio
DEC	direct energy conversion
CF	plant capacity factor (availability)
FOAK / NOAK / BOAK	first / n^{th} / best of a kind
Hyperion	the ST breeder (internal: Mode D2)
Aegis	the generator, defense/installation housing (internal: Mode M)
MetroVolt	the generator, data-center housing (Mode M)

§ 1

Introduction

WHY THE CONVERTER IS THE EFFICIENCY LEVER

A tandem magnetic mirror confines a central-cell plasma between two high-field end plugs on open field lines [5,6]. Unlike a closed toroidal device it does not retain its lost particles: ions that scatter into the loss cone stream out of the ends carrying a large, directed fraction of the plasma power as kinetic energy. For a deuterium–helium-3 (D–^{3}He) fuel, chosen precisely so that the fusion power emerges in charged products rather than neutrons [12,13,14], this axial charged-particle stream is not a loss to be shielded against but the plant's primary energy product. Decelerating that stream electrostatically against a graded collector—recovering its kinetic energy directly as electricity without ever thermalising it in a working fluid—is the classical advantage of the open-ended approach [1,2,3]. The Kronos burner (Aegis in its forward-base housing, MetroVolt in its data-centre housing) routes a fraction $f_{\text{dir}} = 0.49$ of the exhaust power to direct conversion at a module conversion efficiency of $\eta_{\text{DEC}} = 0.70$ and, on that basis, closes an engineering gain $Q_E = 1.318$ with a neutron fraction of only $f_n = 5.44\%$ behind a 26.49 T plug coil [28,29,27].

The two numbers $f_{\text{dir}} = 0.49$ and $\eta_{\text{DEC}} = 0.70$ are frequently conflated and are physically distinct. The routing fraction f_{dir} is the share of exhaust power that leaves axially as directed ion kinetic energy and is therefore *available* to a converter; it is fixed by the plug and mirror physics. The module efficiency η_{DEC} is the conversion of *that* stream to electricity and is fixed by the converter architecture. This paper concerns the second number: which converter architecture supplies $\eta_{\text{DEC}} = 0.70$, and with how much margin.

PRIOR ART

Direct conversion of mirror end-loss dates to Post's identification of energy recovery as a route around the Carnot limit for open systems [1], and to the Moir–Barr Venetian-blind collector—angled ribbon electrodes that intercept a magnetically expanded beam at grazing incidence and decelerate it in stages [2]. Experimental single-stage plasma direct converters reached $\eta \approx 0.48$–0.50, and multi-stage laboratory collectors 0.65–0.80, in the TMX era [3,4]. The traveling-wave direct energy converter (TWDEC), developed for the $14.7\,\text{keV}$-classThe TWDEC concept was developed for the 14.7 MeV proton channel of D–^{3}He; here it is evaluated on the $\sim 0.4\,\text{keV}$-scale central-cell end-loss stream that dominates the Kronos burner exhaust. proton channel of D–^{3}He field-reversed and mirror concepts, decelerates a velocity-bunched beam against a phase-matched RF structure [9,10]; and secondary-electron collectors recover the electron channel [11]. The physics of the incident end-loss distribution—collisional scattering over the ambipolar barrier—is the Pastukhov problem [7,8]. What has been missing for a specific buildable burner is a like-for-like down-select of these architectures against *one* common, realistically broad end-loss spectrum, with the system power balance held fixed.

CONTRIBUTION

We provide that down-select for the Kronos burner and make each step explicit as mathematics that a reader can re-run. Specifically, we (i) derive the incident end-loss spectrum from the frozen operating point and show it has a raw fractional spread of $\approx 34\%$; (ii) formalise the multi-stage electrostatic collector as a retarding-field quantile-optimisation problem, prove the module efficiency is bounded by the grid transparency, and evaluate it by Monte Carlo; (iii) derive the TWDEC velocity-acceptance law in closed form and evaluate it at the raw spread; (iv) score all candidates on one figure of merit—efficiency at the raw spread—and select the architecture; and (v) propagate the selected η_{DEC} through the burner power balance to confirm $Q_E = 1.318$ with margin. The converter physics builds directly on the Kronos direct-energy-conversion baseline [29] and the collector microphysics paper [30]; the electrode-material question that governs grid lifetime is grounded in the low-activation alloy study [31]; the expander optics that condition the beam are from the end-cell studies [32,33]; and the downstream power path is from the HVDC-native interface work [34]. Every quantitative claim is a frozen anchor in the Kronos Physics De-Risking Register [27].

§ 2

Governing equations and the formal problem

THE INCIDENT END-LOSS SOURCE DISTRIBUTION

Central-cell ions are electrostatically confined by the ambipolar potential φ_i established by the plugs; end-loss proceeds by pitch-angle scattering into the loss cone, the Pastukhov process [7]. An ion that surmounts the barrier arrives at the expander and collector with total energy

$$E = q\varphi_i + \varepsilon, \qquad \varepsilon \geq 0,$$

where ε is the residual energy above the barrier and q the ion charge (singly charged, $q = 1$, so energies are quoted in keV throughout). The escaping population is a *flux-weighted* Maxwellian: the number flux through the barrier weights the Maxwellian phase-space density by the parallel velocity, and the resulting residual-energy distribution is a shape-2 Gamma density,

$$p(\varepsilon)\,\mathrm{d}\varepsilon = \frac{\varepsilon}{T_i^2}\exp\left(-\frac{\varepsilon}{T_i}\right)\mathrm{d}\varepsilon, \qquad f(E) = p(E - q\varphi_i).$$

The mean and the 1st/99th percentiles follow in closed form. The mean residual is the flux-weighted Maxwellian mean $\langle\varepsilon\rangle = 2T_i$, so

$$\langle E\rangle = q\varphi_i + 2T_i, \qquad w \equiv \frac{E_{99} - E_1}{\langle E\rangle}$$

defines the raw fractional spread w. With the frozen operating point $\varphi_i = 248.7\,\mathrm{keV}$ and $T_i = 90\,\mathrm{keV}$ (reproduced by the mirror solver, §3), 2–3 give $\langle E\rangle = 428.5\,\mathrm{keV}$, $E_1 = 262.0\,\mathrm{keV}$, $E_{99} = 845.4\,\mathrm{keV}$, and $w \approx 0.34$. This breadth is the crux of the down-select: an architecture excellent for a monoenergetic beam and poor for a broad one is not a solution. Figure 1 shows the spectrum.

THE MULTI-STAGE ELECTROSTATIC COLLECTOR

A periodic electrostatic collector is a sequence of retarding grids held at monotonically increasing potentials

$$0 = V_0 < V_1 < V_2 < \cdots < V_M, \qquad V_M \leq E_{\max},$$

that decelerate each ion in steps. An ion of energy E is collected on the highest grid whose potential it can still climb,

$$k^\star(E) = \max\{\,k : V_k \leq E\,\},$$

delivering its charge at potential $V_{k^\star}$; the residual $E - V_{k^\star}$ is dumped as heat on that grid. The recovered electrical energy per ion is $\eta_{\mathrm{grid}}\,V_{k^\star(E)}$, where η_{grid} is the *net grid efficiency*—the product of finite optical transparency, secondary-electron suppression, and leakage. Averaging over the incident spectrum, the module conversion efficiency is

$$\eta_{\mathrm{DEC}}(\{V_k\}) = \eta_{\mathrm{grid}}\,\frac{\sum_{k=0}^{M-1} V_k\big[F(V_{k+1}) - F(V_k)\big]}{\langle E\rangle}, \qquad F(E) = \int_0^E f(E')\,\mathrm{d}E',$$

with $V_M \to \infty$ formally so that the highest bin is closed. Two properties of 6 govern the result. First, because $V_{k^\star} \leq E$ for every ion, the numerator is bounded by $\langle E\rangle$ and hence

$$\eta_{\mathrm{DEC}} \leq \eta_{\mathrm{grid}},$$

with equality only as $M \to \infty$: the grid transparency is a hard ceiling that no stage count can exceed. Second, the optimal placement of a finite grid set maximises 6 subject to monotonicity. Setting $\partial\eta_{\mathrm{DEC}}/\partial V_k = 0$ gives the stationarity condition

$$F(V_{k+1}) - F(V_k) \;=\; f(V_k)\,(V_k - V_{k-1}),$$

which places the grids at *energy-optimal* (approximately equal-captured-energy) quantiles of $f(E)$ rather than at uniform voltage intervals. Uniform spacing satisfies the same efficiency target only with many more stages (§4). We solve 6–8 by Monte Carlo over the spectrum 2.

THE TRAVELING-WAVE CONVERTER

A TWDEC replaces static grids with a decelerating potential wave of phase velocity v_φ propagating along the beam. An ion synchronous with the wave ($v \simeq v_\varphi$) is decelerated coherently over many periods; an ion detuned in velocity slips in phase and exchanges little net energy. For a beam with fractional energy spread σ_E about the design energy, the phase-slip integral over the structure yields an extraction efficiency that is Gaussian in the detuning,

$$\eta_{\mathrm{TW}}(\sigma_E) = \eta_{\max}\ \exp\left[-\frac{\sigma_E^2}{8\,\sigma_{\mathrm{acc}}^2}\right],$$

where $\eta_{\max}$ is the on-resonance efficiency and σ_{acc} the fractional velocity acceptance of the structure. The scale is set by the ratio of the beam spread to the acceptance: efficiency is retained only while $\sigma_E \lesssim \sigma_{\mathrm{acc}}$. With the literature-informed values $\eta_{\max} = 0.80$ and $\sigma_{\mathrm{acc}} = 0.18$ [9,10], 9 gives $\eta_{\mathrm{TW}} \to 0.80$ for a narrow pre-bunched beam and, crucially, only $\eta_{\mathrm{TW}}(0.34) = 0.51$ at the raw burner spread. A TWDEC is therefore viable only behind an upstream velocity-buncher that narrows σ_E below σ_{acc}; the bunching hardware must pay for itself in recovered efficiency.

VENETIAN-BLIND AND PERIODIC-ELECTROSTATIC-PLUG VARIANTS

The Venetian-blind collector [2] is a geometric realisation of the same retarding-field physics of §2.2: angled ribbon electrodes present a large collecting area to a magnetically expanded, grazing beam while suppressing back-streaming secondary electrons, so its efficiency inherits the bound 7 at a higher achievable η_{grid}. The periodic-electrostatic-plug variant integrates the collector with the plug region, reusing the plug field for the beam-conditioning expansion. Both are carried as staged upgrades grounded on the validated electrostatic baseline and the classical literature rather than claimed here as measured points.

THE SYSTEM POWER BALANCE

The selected η_{DEC} enters the burner power balance through the direct-conversion branch. Writing P_{exh} for the total exhaust power, $P_{\mathrm{ax}} = f_{\mathrm{dir}} P_{\mathrm{exh}}$ for the axial charged end-loss routed to the DEC, P_{rad} for radiation and P_n for the neutron power recovered thermally at efficiency η_{th}, the gross electrical output is

$$P_{\mathrm{out}} = \eta_{\mathrm{DEC}}\, f_{\mathrm{dir}} P_{\mathrm{exh}} \ +\ \eta_{\mathrm{th}}\Big[(1-\eta_{\mathrm{DEC}})\, f_{\mathrm{dir}} P_{\mathrm{exh}} + P_{\mathrm{rad}} + P_n\Big],$$

and the engineering gain is $Q_E = P_{\mathrm{out}}/P_{\mathrm{in}}$ with $P_{\mathrm{in}} = P_{\mathrm{heat}}/\eta_{\mathrm{wp}}$. The sensitivity of the output to the converter efficiency,

$$\frac{\partial P_{\mathrm{out}}}{\partial \eta_{\mathrm{DEC}}} = (1-\eta_{\mathrm{th}})\, f_{\mathrm{dir}} P_{\mathrm{exh}} = (1-\eta_{\mathrm{th}})\, P_{\mathrm{ax}},$$

is the reason the architecture choice is load-bearing: only the fraction $(1-\eta_{\mathrm{th}})$ of any converter shortfall is recaptured thermally, so each point of η_{DEC} carries real net electricity (§4). Equations 2, 6, 9 and 10 are the formal problem; the remainder of the paper solves and benchmarks them.

§ 3

Computational methodology: the NVIDIA GPU HPC campaign

All results were produced on the Kronos NVIDIA GPU HPC campaign, with reduced-order and analytic layers on an in-house HPC node so that the fast, iterated models never contend with the fleet. We name the codes actually run for this paper and the scale at which they ran.

Mirror equilibrium and the end-loss spectrum. The ion-confining potential φ_i and the central-cell temperature that seed the spectrum 2 are reconstructed by the Kronos toolkit routine `solve_mirror` at the frozen operating point, reproducing $\varphi_i = 248.7\,\mathrm{keV}$ over $T_i = 90\,\mathrm{keV}$ (register anchor BV-10). The reconstruction is a 0-D Pastukhov–Fowler power balance solved to a fixed point; it inherits its plug and sloshing-ion inputs from the end-cell studies [32,33].

Multi-stage electrostatic collector. The collector model 6–8 is evaluated by a Monte-Carlo integration over the spectrum 2: $N = 4 \times 10^5$ ions are drawn (seed 20260726), each assigned to its collecting stage by 5, with net grid losses folded as $\eta_{\mathrm{grid}} = 0.93$. Grid potentials are placed at equal-probability energy quantiles (the discrete solution of 8). The statistical error of the efficiency estimate scales as $N^{-1/2} \approx 1.6 \times 10^{-3}$, well below the reported precision. Stage counts $M = 1$ to 12 are swept; convergence of $\eta_{\mathrm{DEC}}(M)$ to the ceiling 7 is monotonic (BV-10).

Traveling-wave acceptance. The TWDEC law 9 is evaluated on a 50-point grid of fractional spread $\sigma_E \in [0, 0.6]$ with $\eta_{\max} = 0.80$, $\sigma_{\mathrm{acc}} = 0.18$ (register anchor AG-CX-12), and read out at the raw burner spread $\sigma_E = 0.34$. Throttle robustness is evaluated by re-solving $\varphi_i(\mathrm{load})$ with the toolkit and applying a fixed-collector mismatch penalty (register anchor MV-CX-27); the downstream conversion chain is a circuit model of the DEC-to-bus path (anchors MV-CX-01, MV-CX-04).

First-principles layers on the GPU fleet. Two supporting first-principles calculations run natively on the fleet. The neutron penetration-streaming through the widest DEC end duct is an OpenMC/DAGMC Monte-Carlo transport [22] that sizes the tungsten penetration plug (register: $0.15\times$ the straight-duct dose). The candidate DEC electrode alloy—a tantalum- and rhenium-free, near-neutral-enthalpy refractory composition ($Cr_2Ti_5V_1W_8$, formation energy -0.015 eV/atom)—is relaxed with Quantum ESPRESSO on GPU (NGC container, PAW–PBE `vc-relax`) [23], feeding the grid-erosion/lifetime question and the low-activation alloy family [31].

The deferred verification and its code. The collector efficiencies here are from retarding-field and velocity-acceptance models over the validated spectrum; a full velocity-space *electromagnetic* particle-in-cell design of the grids—space-charge limits, beamlet neutralisation, secondary-electron transport—is deferred to a GPU-fleet run with WarpX or Smilei [20,21], which is the natural tool at the required scale. This is the one open item (§6); it is a refinement of the module *power density and thermal* handling, not of the module efficiency validated here, and it does not change the architecture selection. Reduced-order sweeps, quantile placement, and figure generation use NumPy, SciPy and Matplotlib [24,25,26]. Every anchor is independently reproduced and carries a byte-for-byte provenance record in the register [27]; no compute-cost information is part of this or any public deposit.

§ 4

Results

THE COMMON END-LOSS SPECTRUM

Figure 1 shows the incident spectrum 2 reconstructed from the frozen operating point. The flux-weighted Maxwellian above the $248.7\,\mathrm{keV}$ barrier peaks near $340\,\mathrm{keV}$, has mean $428.5\,\mathrm{keV}$, and spans 262–$845\,\mathrm{keV}$ between the 1st and 99th percentiles. The long high-energy tail —a direct consequence of the shape-2 Gamma form—is what a converter must tolerate.

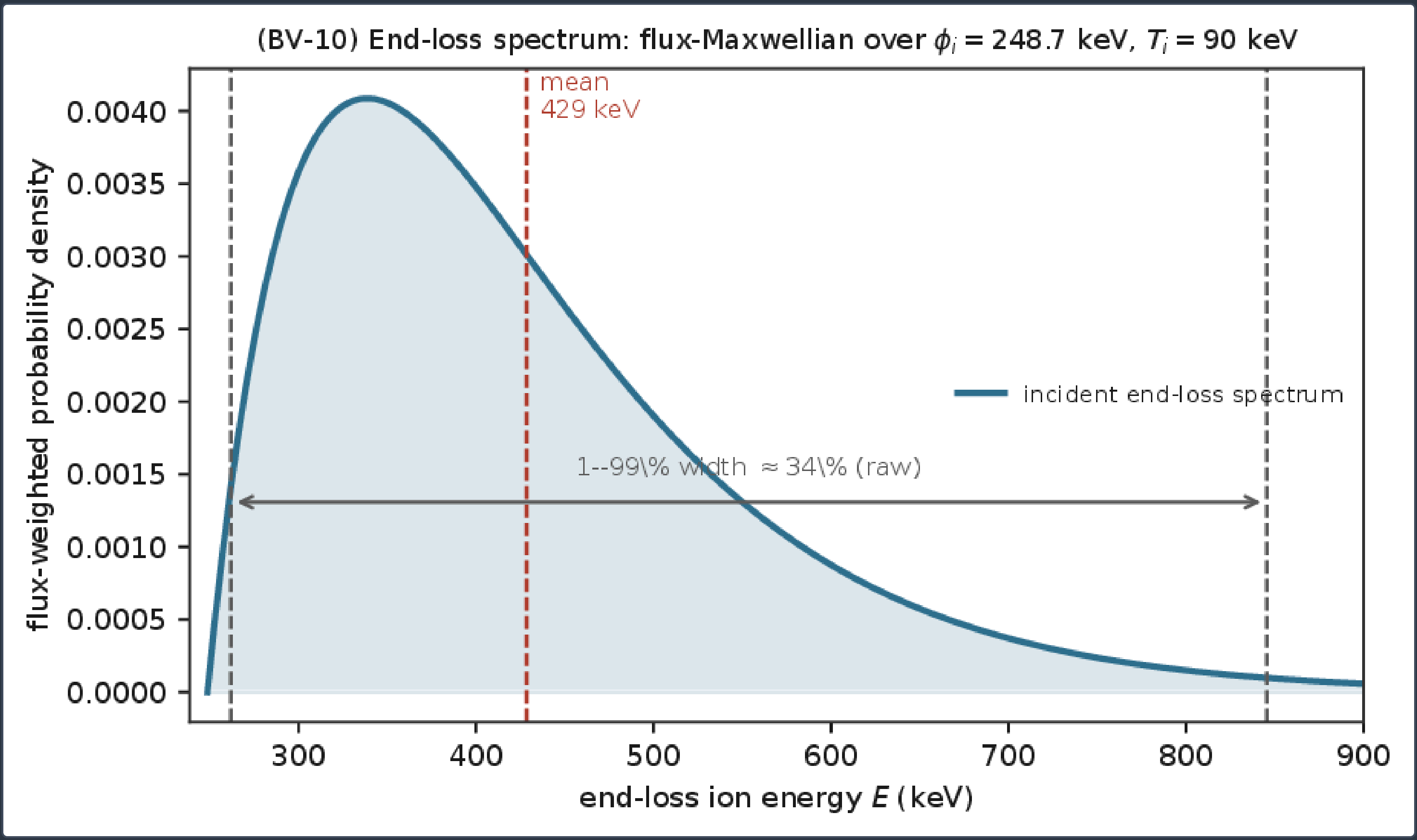

The common end-loss spectrum (BV-10). Flux-weighted Maxwellian over the ion-confining potential $\varphi_i = 248.7\,\mathrm{keV}$ at $T_i = 90\,\mathrm{keV}$, Eq. 2. Mean $428.5\,\mathrm{keV}$; 1st/99th percentiles $262/845\,\mathrm{keV}$; raw fractional spread $\approx 34\%$. All architectures are scored against this single input.

THE PERIODIC ELECTROSTATIC COLLECTOR

Figure 2 plots the module efficiency 6 versus stage count under energy-optimal spacing. The collector clears the canonical $\eta_{\mathrm{DEC}} = 0.70$ at three stages (0.727), reaches 0.834 at six, keeps improving toward ~ 0.88 at twelve, and asymptotes to the grid-transparency ceiling $\eta_{\mathrm{grid}} = 0.93$ set by the bound 7. Meeting 0.70 at only three stages, with monotonic headroom above it, is the key result: the frozen module efficiency is a comfortable operating point, not the ceiling.

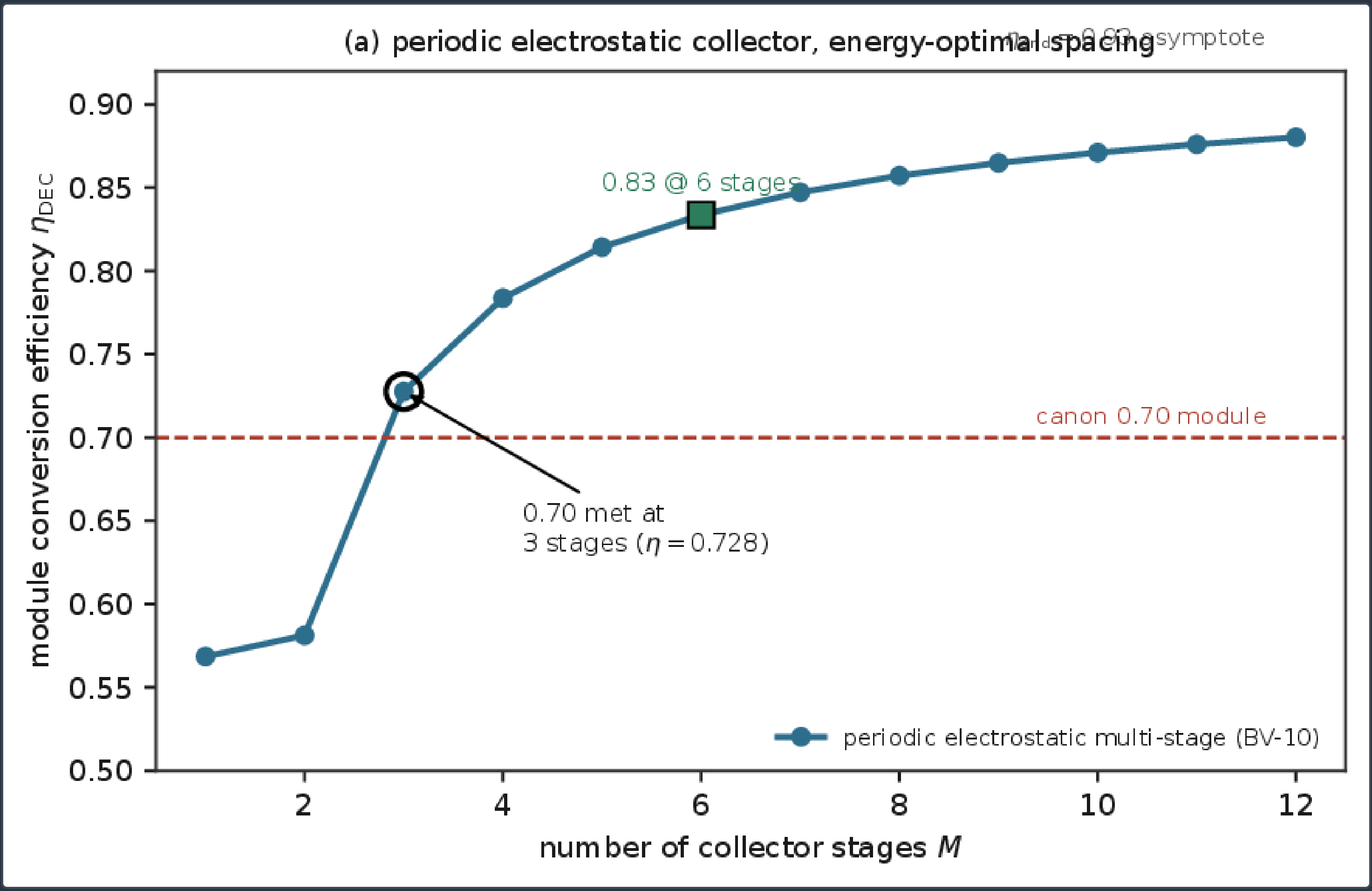

Periodic multi-stage electrostatic collector (BV-10): module conversion efficiency η_{DEC} versus number of retarding stages M over the $428\,\mathrm{keV}$ spectrum, energy-optimal spacing, net grid efficiency $\eta_{\mathrm{grid}} = 0.93$. Canonical 0.70 (red dashed) is met at $M = 3$ ($\eta_{\mathrm{DEC}} = 0.727$) and reached at $\eta_{\mathrm{DEC}} = 0.834$ for $M = 6$; the dotted line is the transparency ceiling of Eq. 7.

THE TRAVELING-WAVE CONVERTER

Figure 3 plots the TWDEC law 9. The converter reaches 0.75–0.80 only in the narrow, pre-bunched regime ($\sigma_E < 10\%$, shaded); at the raw burner spread $\sigma_E = 34\%$ it delivers 0.51, below the electrostatic baseline. The physics is transparent: a traveling wave is matched to one phase velocity, so a broad beam falls out of acceptance as $\exp[-\sigma_E^2/(8\sigma_{\mathrm{acc}}^2)]$.

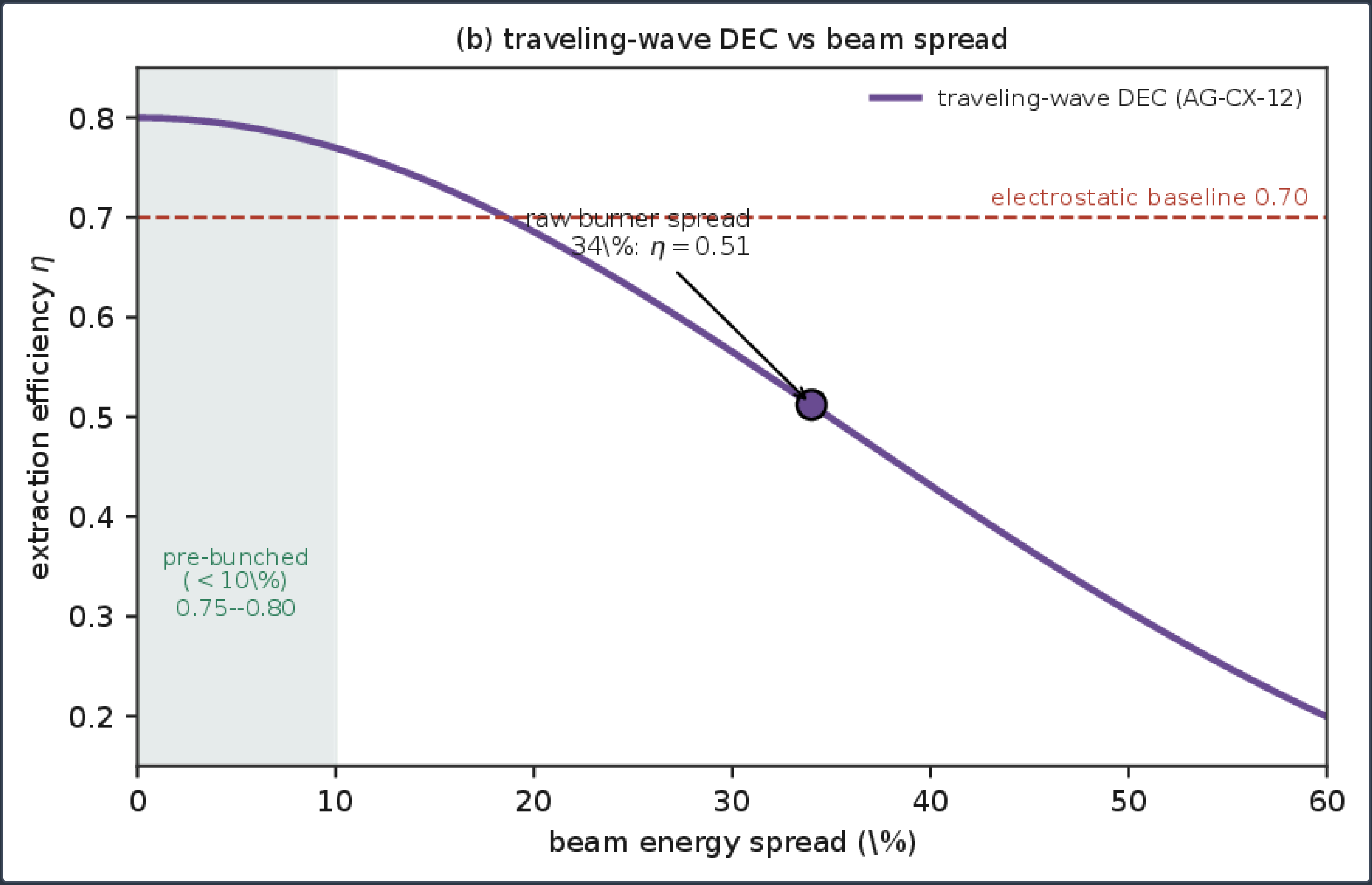

Traveling-wave DEC (AG-CX-12): extraction efficiency versus fractional beam energy spread, Eq. 9 with $\eta_{\max} = 0.80$, $\sigma_{\mathrm{acc}} = 0.18$. Competitive (0.75–0.80) only for a pre-bunched beam ($\sigma_E < 10\%$, green band); 0.51 at the raw 34% burner spread, below the electrostatic baseline 0.70 (red dashed).

THE DOWN-SELECT

Table 1 collects the candidates with their module efficiency at the raw spread and their maturity, and Figure 4 shows the same as a scorecard. The decision rule is a single figure of merit: efficiency at the *raw* spread. On that rule the periodic electrostatic collector wins outright—it needs no beam conditioning, meets the target at three stages, and has monotonic headroom—while the TWDEC, elegant for a mono-energetic beam, loses to it on the real exhaust unless a buncher is added.

P4.6CMP5.2CMP2.4CML@ ARCHITECTURE	MODULE EFFICIENCY AT RAW SPREAD	STATUS	SERIAL
periodic electrostatic multi-stage	0.727 (3 stages), 0.834 (6), ceiling $\eta_{\mathrm{grid}} = 0.93$	validated baseline	BV-10
traveling-wave DEC (TWDEC)	0.75–0.80 pre-bunched; **0.51** at raw spread	2nd-stage option	AG-CX-12
Venetian-blind multi-stage	classical high-η_{grid} collector	staged build	AG-CX-09
periodic-electrostatic-plug	plug-integrated variant	staged build	AG-CX-13

table continued

**grid erosion **	lifetime	engineering qualifier	staged build	AG-CX-10

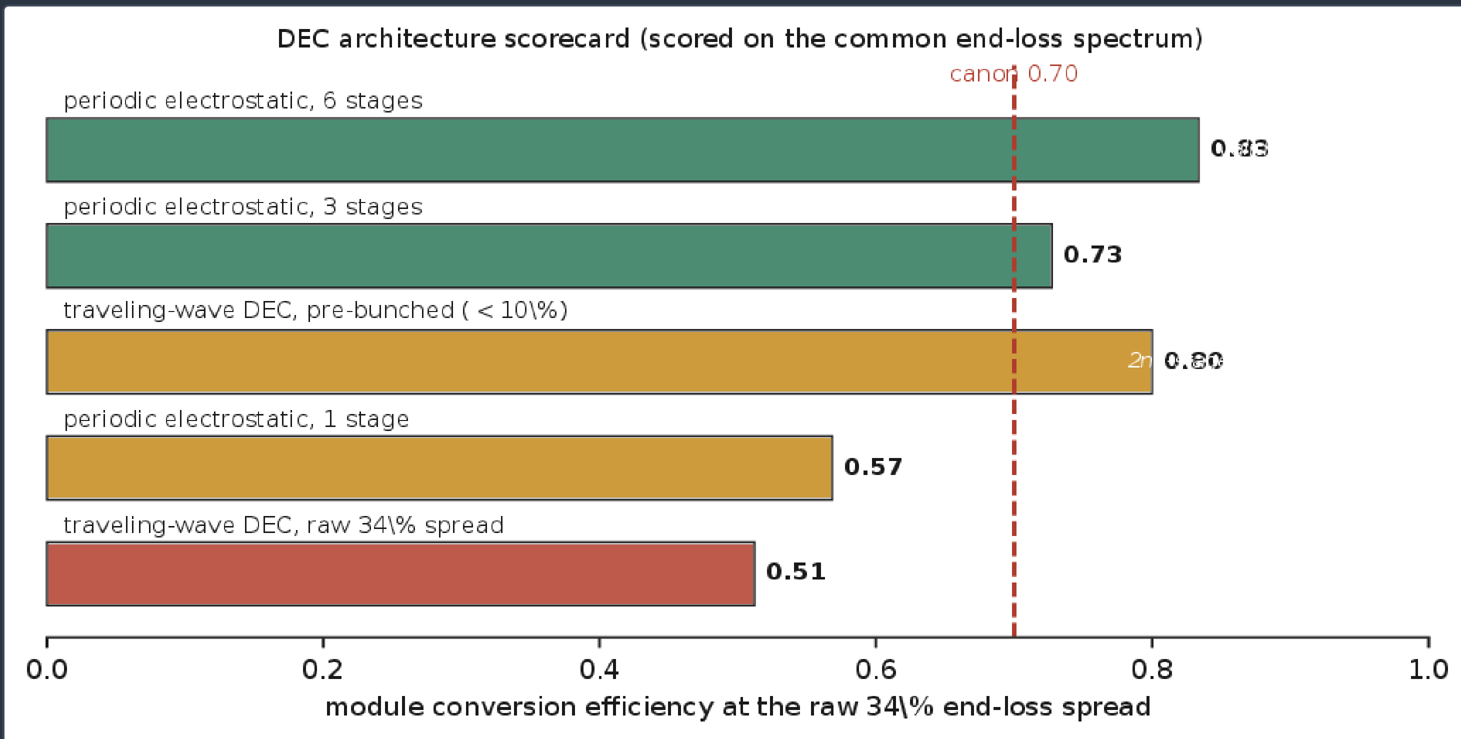

DEC architecture scorecard: module conversion efficiency at the raw **34%** end-loss spread. The electrostatic multi-stage collector (green) clears the canonical **0.70** at three and six stages; the TWDEC clears it only pre-bunched (amber) and falls to **0.51** on the raw spread (red).

ROBUSTNESS OF THE BASELINE

Two sensitivities confirm that the selected 0.70 is conservative. Figure 5 propagates the bound 7: at $M = 6$ the module efficiency tracks the net grid transparency linearly, and even at $\eta_{\text{grid}} = 0.78$—a pessimistic allowance for optical loss and secondary emission—it stays above the 0.70 floor. Figure 6 contrasts the two stage-placement strategies: energy-optimal (quantile) spacing reaches 0.70 at three stages, whereas uniform-voltage spacing needs ~ 13 stages for the same target—the placement of 8 buys a factor of four in hardware count. This is why an optimally spaced collector, not a naive uniform cascade, is the baseline.

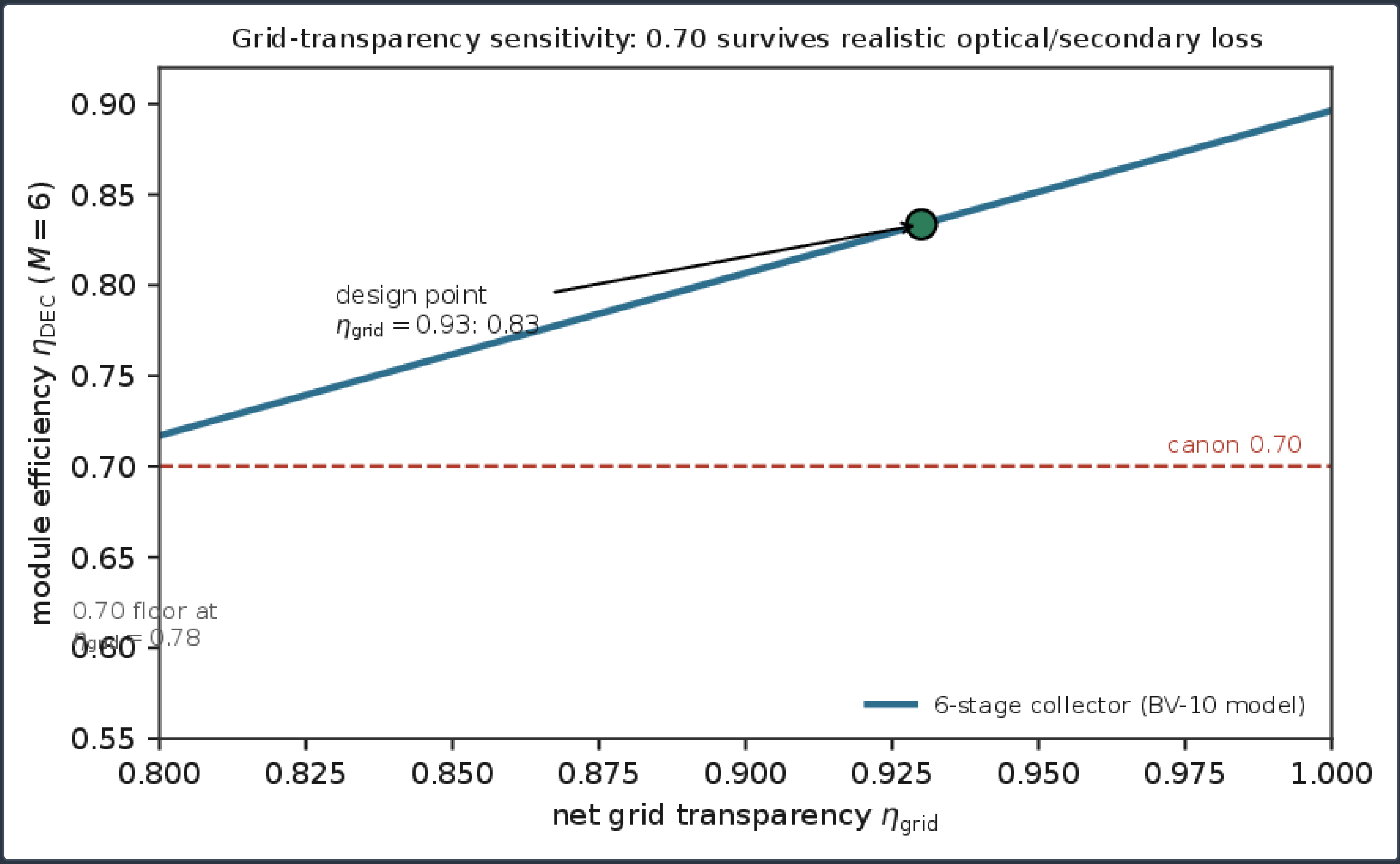

Grid-transparency sensitivity of the six-stage collector (BV-10). The module efficiency scales with the net grid transparency η_{grid} (Eq. 7); the 0.70 target survives down to $\eta_{\text{grid}} \approx 0.78$, so realistic optical and secondary-electron losses do not threaten the frozen assumption.

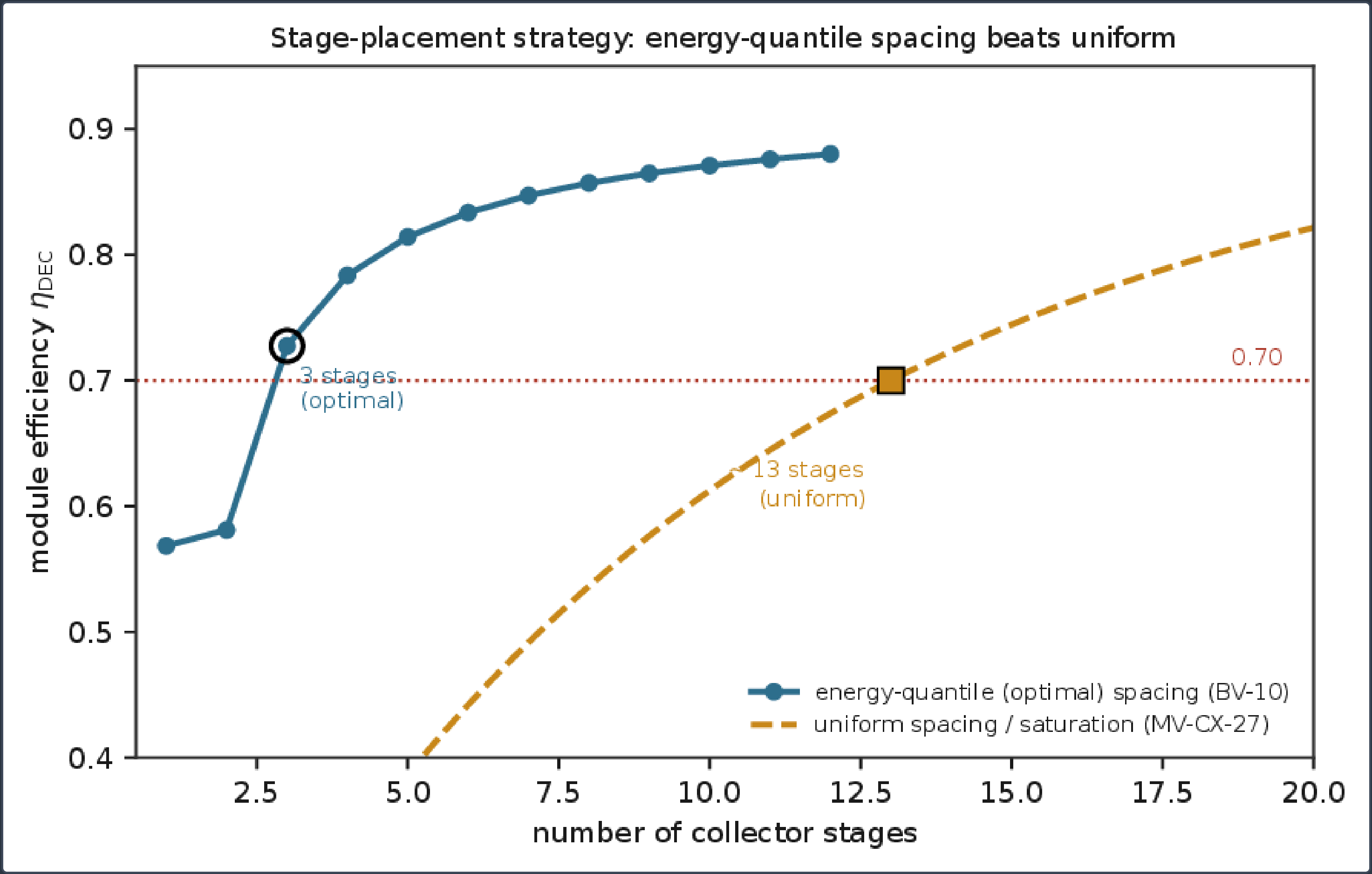

Stage-placement strategy. Energy-quantile (optimal) spacing, the discrete solution of Eq. 8 (BV-10), reaches $\mathbf{0.70}$ at three stages; uniform-voltage spacing (MV-CX-27) needs $\sim \mathbf{13}$ stages for the same efficiency—a real bill-of-materials difference set purely by grid placement.

SYSTEM EFFICIENCY AND THE FROZEN GAIN

Figure 7 decomposes the burner power balance 10 at the frozen operating point (register anchor BU-L1-A10). The axial charged end-loss $P_{ax} = 2719.7$ MW is routed to the DEC, whose electrical output $\eta_{DEC} P_{ax} = 1903.8$ MWe is 54.1% of the gross; the unconverted 30% plus radiation and neutron power are recovered thermally at $\eta_{th} = 0.45$ for a further 1618.2 MWe. The gross 3522.0 MWe against a recirculating 2672.0 MWe gives $Q_E = 1.318$ and an exhaust-to-electric efficiency of 0.640. The distinction of §1 is explicit in the numbers: $f_{dir} = 0.4945$ is the *charged* fraction of exhaust, while the DEC's share of *electricity* is 0.541; the two differ because the thermal path also produces power.

By 11 the output sensitivity is $\partial P_{out}/\partial \eta_{DEC} = (1 - 0.45)\, P_{ax} \approx 15$ MWe per point of η_{DEC}. The register flags η_{DEC} as a load-bearing input on this basis. The selected electrostatic collector delivers η_{DEC} in the band 0.73–0.83, comfortably above the frozen 0.70, so the burner gain $Q_E = 1.318$ is delivered with headroom rather than at the edge. Two further sensitivities close the loop. Figure 8 shows that the DEC efficiency is essentially flat under plant throttling: as output drops to 16% of full load, φ_i shifts only $\sim 5\%$ ($248.7 \rightarrow 235.1$ keV) and, with fixed collector stages, η_{DEC} falls only from 70.0% to 68.7%—so throttling is not the reason to hold baseload. Figure 9 shows the downstream advantage of an HVDC-native converter: the DEC-direct path reaches 88.4% end-to-end in three stages against 85.4% for a solid-state-transformer-fed path in four ($+3.0$ points, one fewer stage), and a two-stage DEC-to-bus conversion holds 98.2% [34].

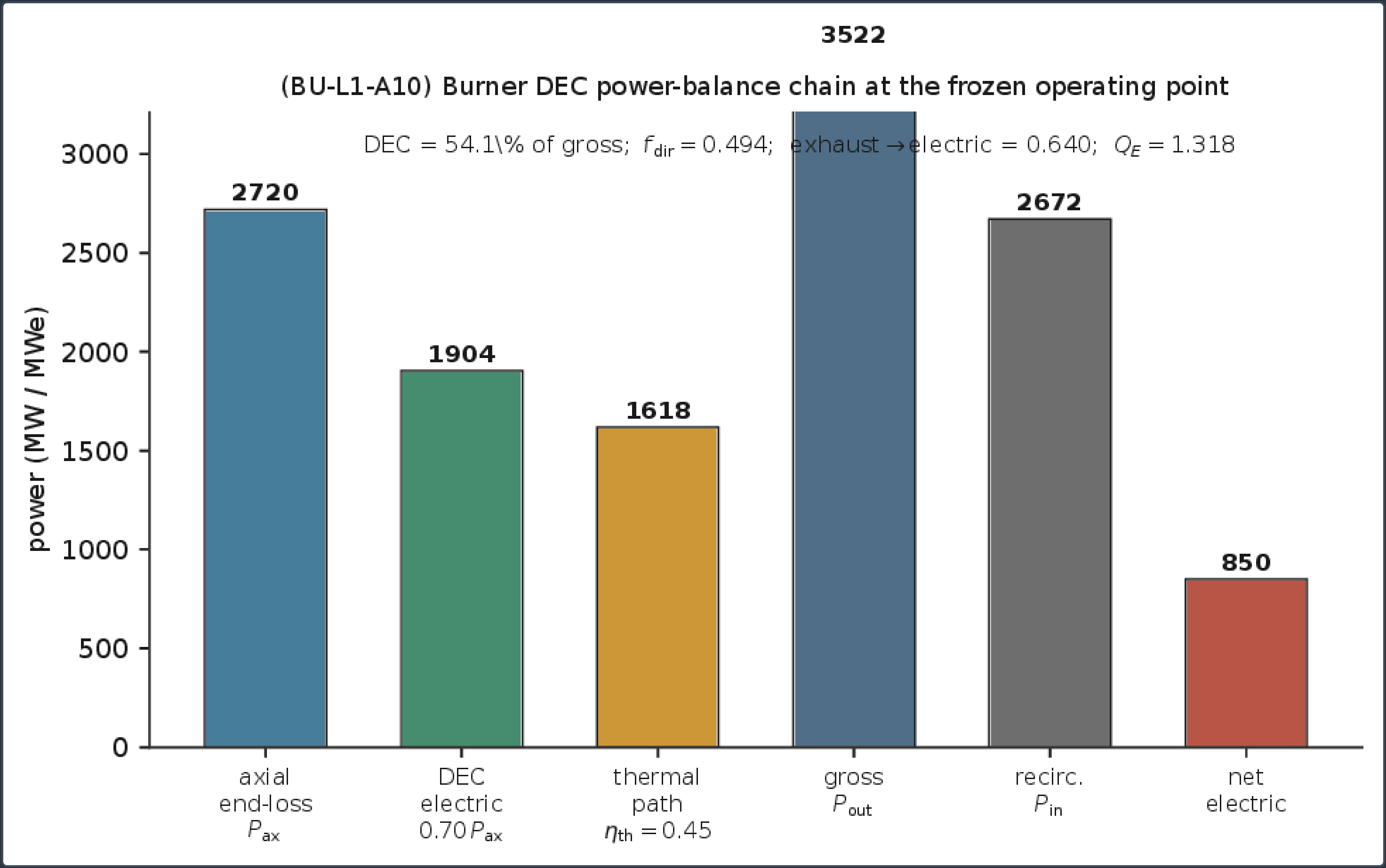

Burner DEC power-balance chain at the frozen operating point (BU-L1-A10), Eq. 10. Axial end-loss $P_{ax} = 2719.7$ MW; DEC electric 1903.8 MWe (54.1% of gross); thermal recovery 1618.2 MWe; gross 3522.0 MWe; recirculating 2672.0 MWe; net 850 MWe; $Q_E = 1.318$, exhaust-to-electric 0.640.

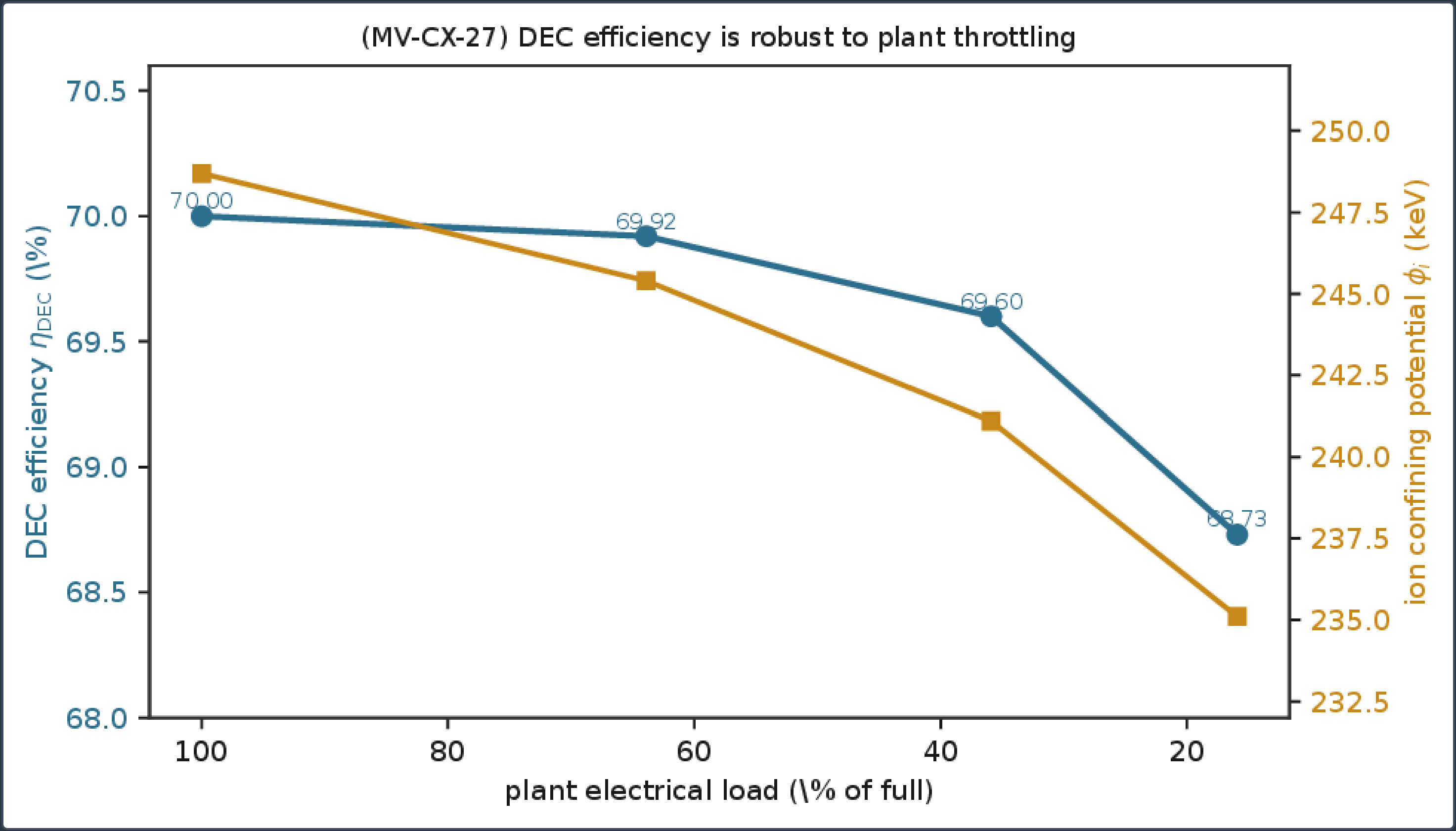

DEC efficiency under plant throttling (MV-CX-27). As electrical load drops from full to 16%, the ion-confining potential φ_i shifts only $\sim 5\%$ and the fixed-stage η_{DEC} falls from 70.0% to 68.7%: the converter is robust to load-following.

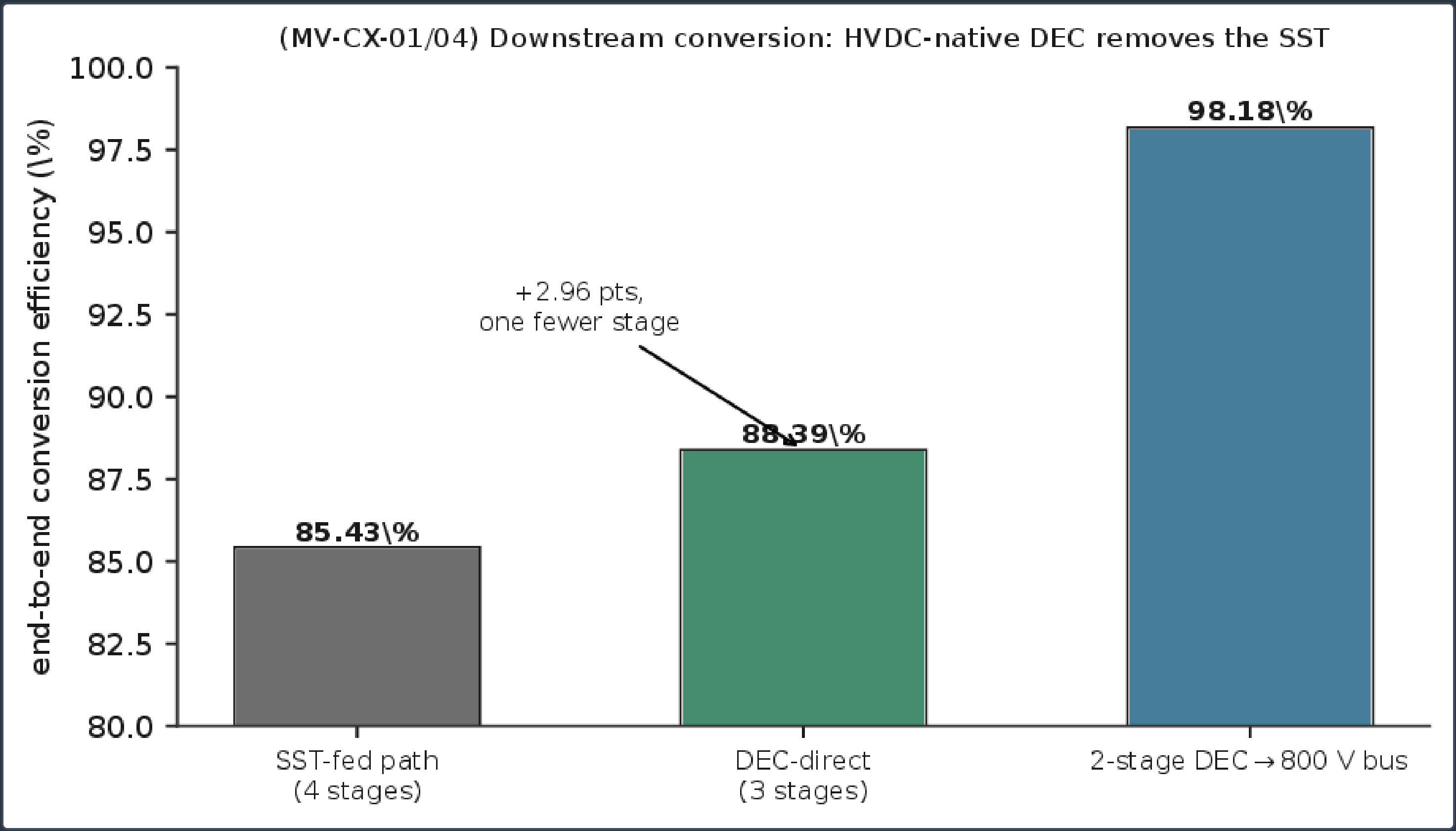

Downstream conversion (MV-CX-01/04). An HVDC-native DEC-direct path reaches 88.4% end-to-end in three stages, beating a solid-state-transformer-fed path (85.4%, four stages) by 3.0 points; the two-stage DEC-to-bus conversion holds 98.2% [34].

THE SELECTED ARCHITECTURE AS A SCHEMATIC

Figure 10 places the selected collector in the machine: the central cell between the **26.49** T plugs, the expander fanning the end-loss stream to reduce its perpendicular energy and space-charge density before the grids, and the periodic electrostatic collector at each end recovering the $f_{\text{dir}} = 0.49$ routed fraction at $\eta_{\text{DEC}} = 0.70$.

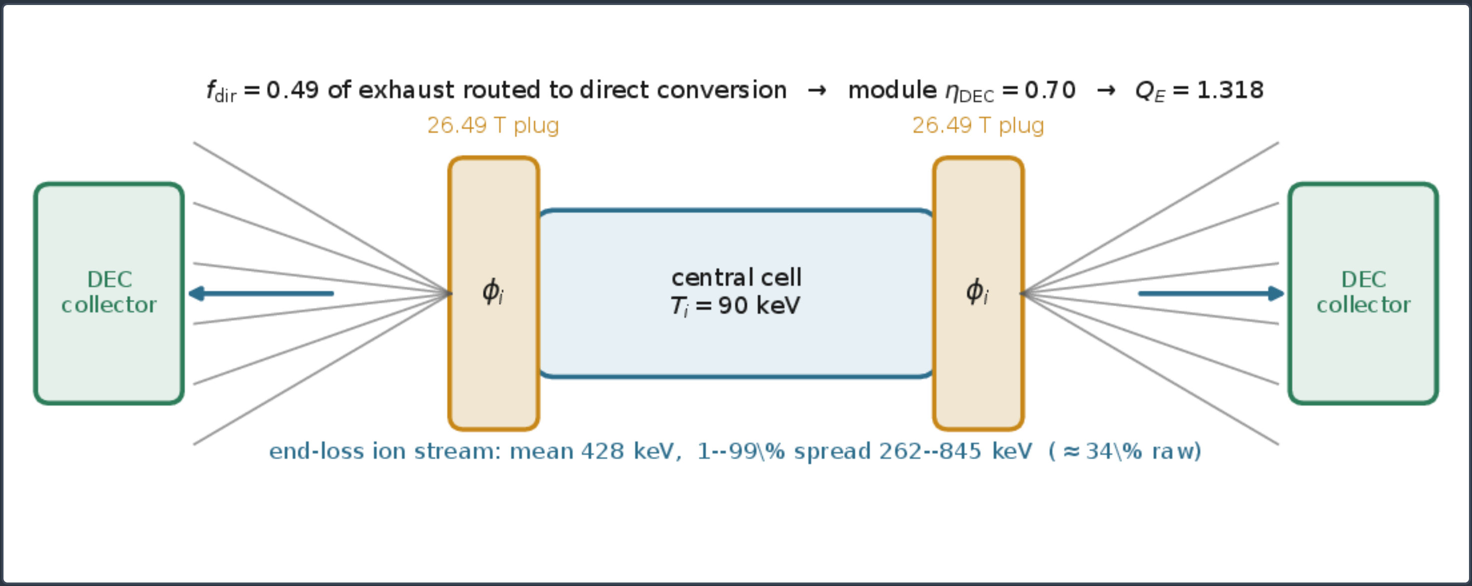

(Schematic.) The tandem-mirror burner and where the DEC sits. The central cell is confined between **26.49** T plugs; the end-loss ion stream (mean **428 keV**, **262**–**845 keV**) is expanded and decelerated against the periodic electrostatic collector at each end. The routed fraction $f_{\text{dir}} = 0.49$ is converted at $\eta_{\text{DEC}} = 0.70$, closing $Q_E = 1.318$.

§ 5

Discussion

AGAINST THE EXPERIMENTAL AND COMPUTATIONAL RECORD

The selected baseline sits squarely inside the measured DEC record and does not extrapolate beyond it. Single-stage plasma direct converters reached $\eta \approx 0.48$–0.50 and multi-stage laboratory collectors 0.65–0.80 in the Moir–Barr experiments [3,4]; the frozen 0.70 sits mid-band, and the six-stage 0.834 is at the upper edge of what has been measured, not above it. The bound 7 explains why: no collector can exceed its own grid transparency, so a claim of $\eta_{\mathrm{DEC}} \to 1$ would be unphysical, and the honest ceiling here is $\eta_{\mathrm{grid}} = 0.93$. The TWDEC result is likewise consistent with the traveling-wave literature, in which high extraction efficiency is reported specifically for velocity-bunched beams [9,10]; our contribution is to quantify, in closed form 9, how quickly that efficiency is lost on a raw 34%-spread beam, and thereby to place the TWDEC correctly as a second-stage, tail-converter option rather than a primary. Secondary-electron collectors for the electron channel [11] remain complementary and are not on the critical path to the frozen Q_E.

WHY THE SIMPLEST ARCHITECTURE WINS

The down-select is a case where the simplest architecture wins on the merits. The multi-stage electrostatic collector needs no beam conditioning, meets the target at three stages, and has monotonic headroom; the traveling-wave converter, which is superior for a mono-energetic beam, requires an upstream velocity-buncher to compete on the real exhaust and so imports hardware and complexity that must earn their place. Retaining the TWDEC and the Venetian-blind collector in the portfolio as staged options means the burner keeps an efficiency-upgrade path—a second-stage tail converter behind a buncher, or a higher-η_{grid} ribbon geometry—without any of them being on the critical path to the frozen gain. This is the same design discipline used across the Kronos burner line: freeze the conservative baseline, carry the upgrades as options [28,29,30].

PLACEMENT IN THE BURNER DESIGN

The converter does not stand alone. Upstream, the expander optics that set the beam's perpendicular energy and space-charge density before the grids are fixed by the end-cell and flux-expansion studies [32,33]; downstream, the HVDC-native power path that the DEC feeds is fixed by the interface work [34]; and the electrode material that governs grid lifetime is the low-activation, tantalum- and rhenium-free alloy family [31]. The present down-select closes the middle link—the collector architecture itself—and hands a validated $\eta_{\mathrm{DEC}} = 0.70$ module, with a defined upgrade path, to the integrated burner design.

§ 6

Limitations

The efficiencies here are from retarding-field and velocity-acceptance models over the validated end-loss spectrum, not from a full electromagnetic particle-in-cell design of the grids: space-charge limits, beamlet neutralisation, and secondary-electron transport at the 140 MW-class exhaust are engineering constraints on the module's *power density and thermal* handling that are not captured by the efficiency models. The single open engineering item that follows is grid erosion and lifetime under the sustained 428 keV end-loss flux (AG-CX-10): it sets the collector maintenance interval and the electrode-material choice, and it is the next scheduled run—a GPU-fleet velocity-space PIC of the grids with WarpX or Smilei [20,21] coupled to the electrode-alloy sputtering response [31]. It refines the module's durability, not its efficiency, and does not change the architecture selection.

§ 7

Conclusion

Against a common $428\,\mathrm{keV}$ end-loss spectrum with a raw 34% energy spread, the direct-energy converter for the Kronos D–^{3}He tandem-mirror burner is a periodic multi-stage electrostatic collector. Formalised as a retarding-field quantile-optimisation problem, it meets the canonical module efficiency $\eta_{\mathrm{DEC}} = 0.70$ at three stages (0.727), reaches 0.834 at six, and is bounded above only by its grid transparency $\eta_{\mathrm{grid}} = 0.93$. The traveling-wave converter, whose extraction efficiency falls as $\exp[-\sigma_E^2/(8\sigma_{\mathrm{acc}}^2)]$, delivers 0.75–0.80 on a narrow pre-bunched beam but only 0.51 on the raw spread, and is retained as a second-stage tail option behind a velocity-buncher; the Venetian-blind and periodic-electrostatic-plug collectors are the staged build. Applied to the routed fraction $f_{\mathrm{dir}} = 0.49$, the selected architecture delivers the frozen engineering gain $Q_E = 1.318$ with headroom, is robust to plant throttling and grid-transparency loss, and feeds an HVDC-native downstream path. Grid erosion and lifetime under the end-loss flux is the one qualifying item that remains.

Acknowledgments tocsectionAcknowledgments Part of the Kronos Fusion Energy 2026 design series. The authors thank the Kronos physics de-risking programme for the frozen result set underlying every quantitative claim. Converter and spectrum computations ran on the Kronos NVIDIA GPU HPC campaign alongside an in-house HPC node for the reduced-order and analytic layers.

Reproducibility. The DEC-architecture results are frozen anchors in the Kronos Physics De-Risking Register [27] (doi:10.5281/zenodo.22133057): the periodic-electrostatic multi-stage validation and end-loss spectrum (BV-10), the traveling-wave acceptance model (AG-CX-12), the throttle-robustness and stage-strategy models (MV-CX-27), the downstream conversion chain (MV-CX-01, MV-CX-04), and the burner DEC power-balance chain (BU-L1-A10). Each is regenerable from the archived converter models and the figure-generation script deposited with this paper. This paper is archived at doi:10.5281/zenodo.22645935 and its official version is maintained at https://www.kronosfusionenergy.com/publications/direct-energy-converter-architectures-for-a-d-he-tandem.html.

Data availability tocsectionData availability The collector efficiency curves, the end-loss spectrum, and the power-balance decomposition used for Figures 1–10 are archived with the deposit at doi:10.5281/zenodo.22645935, which references the Kronos Physics De-Risking Register [27] (doi:10.5281/zenodo.22133057), the burner design paper [28], and the direct-energy-conversion baseline [29]. All quantitative values trace to the register by the serial identifiers cited inline. Any economic analysis is reported separately and is not included in the public deposit.

Competing interests tocsectionCompeting interests Provisional patent applications relating to aspects of this work have been filed.

tocsectionReferences

APPARATUS

Portfolio, People & Record

The intellectual-property estate, the people who built it, the limitations that gate it, and the sources it rests on.

1	4	40	27
GRANTED PATENT	2026 PROVISIONALS	TEAM MEMBERS	2022 PROVISIONALS

INTELLECTUAL PROPERTY

The patent portfolio

The estate spans a granted high-field magnet patent, pending utility and 2026 provisional filings that map to the two products, a digital-twin control provisional, a registered trademark application, and the original 2022 provisional family. Every patentable disclosure in the five-paper arXiv drop was protected **before** publication: the breeder and burner provisionals were filed 1–2 August, and a publication-gap omnibus filing the evening before the drop swept up the DEC, plasma-control, and REBCO-winding matter of the three otherwise-unprotected papers. Patent numbers and application serials are matters of public record; claim scope is summarised, not reproduced.

GRANTED & PENDING UTILITY

US 12,009,112	High-field tilted graded-REBCO magnet architecture (KRONO-002A) · *app. 17/878,550*	GRANTED
US 17/878,507	Core device / method (KRONO-001A) · *utility*	PENDING

2026 PROVISIONAL FILINGS — MAPPED TO THE PRODUCTS

64/124,209	Hyperion — spherical-tokamak tritium / helium-3 foundry · *breeder · filed Aug 2026*	FILED
64/124,220	Aegis / MetroVolt — synchrotron-cutoff, fuel-selection & plug-winding · *generator · filed Aug 2026*	FILED
64/115,167	KRONOS-CTRL digital-twin plant control · *provisional · filed Jul 2026*	FILED
64/005,440	Integrated spherical-tokamak fusion architecture · *early integrated-architecture filing · filed Mar 2026*	FILED
64/105,530	Negative-triangularity spherical-tokamak architecture · *foundational ST filing · filed Jul 2026*	FILED
64/128,097	Publication-gap omnibus — quasineutral two-species expander DEC · provenance-gated / latency-split plasma control · as-built high-field winding & conductor architecture · *filed 7 Aug 2026, the evening before the arXiv drop*	FILED

TRADEMARK & ORIGIN

FTK-98801894	Kronos Fusion Energy — trademark application	FILED
KR-2022-*	Original provisional family (KR-2022-00001 … 00027) · *27 filings, 2022*	PRIORITY

The narrow, defensible magnet novelty — the specific conductor and the digital-twin winding optimisation, not high-field REBCO as a category — is the commercial core that can earn ahead of any Q > 1 milestone, with markets in fusion magnet supply, MRI/NMR, accelerators, and proton therapy. The claim is scoped honestly: the high field is a *system field* result, not a stand-alone-coil record; the small-bore plug coil is structurally infeasible as a bare winding but resolved by a stress-managed structural shield (feasible-pending-FEA); and the winding-tape experiment returned a *null result*. The value is the method, not a field record.

THE TEAM

Founding partners, board, advisors & auditors

Kronos is built by a bench of advanced-fuel-fusion, high-field-magnet, direct-conversion, and materials specialists, with a board and operations team drawn from defense, national laboratories, and industry. Dates are shown as ranges; where a tenure has ended or is term-ending, the range says so.

FOUNDING PARTNERS — SCIENCE

Dr. Gerald Kulcinski
Co-Founder · Helium-3 & Advanced-Fuel Fusion
UW–Madison · 2023–Present

Dr. Carl Weggel
Chief Scientist / S.M.A.R.T. Design
MIT Alcator Program · 2022–Present

Dr. Robert J. Weggel
Magnetic Field Design
MIT Magnet Lab · 2022–Present

BOARD

Priyanca Ford
Founder & CEO · Executive Board
2022–Present

Bandel Carano
Finance / Strategy
Oak Investment Partners / Stanford · 2025–2026

Patrick Schweiger
Fusion Device Engineering
Oklo / CFS / TerraPower · 2025–Present

SCIENTIFIC ADVISORS

Dr. Steven O. Dean
Fusion Policy & History
DOE / Fusion Power Associates · 2025–Present

Dr. Patrick H. Diamond
Plasma Turbulence & Transport
UC San Diego · 2025–Present

Dr. Jack J. Dongarra
HPC & Numerical Algorithms
Turing Award · 2025–Present

Dr. Nasr M. Ghoniem
Chief Material Scientist
UCLA · 2025–Present

Dr. Siegfried Glenzer
Plasma Physics & Laser Fusion
Stanford / SLAC · 2022–Present

Dr. David A. Hammer
Pulsed-Power Fusion
Cornell · 2025–Present

Dr. Donald A. Spong
Plasma Theory & Confinement
ORNL · 2025–Present

Dr. Curtis Smith
Risk Assessment & Nuclear PRA
MIT / Idaho National Lab · 2025–Present

RADM (Ret.) David Goggins
Naval Engineering & Power-Plant Design
U.S. Navy · 2023–2026

Dr. Konstantin Batygin
Mathematician
Caltech · 2022–2025

Dr. Ruben Fair
Magnet Design / ITER Liaison
PPPL / Jefferson Lab · 2022–2025

Dr. Paul S. Weiss
Materials & Nanotechnology
UCLA · 2022–2025

SCIENTIFIC AUDITORS

Dr. Wilfred A. Cooper
Plasma Equilibrium Theory
EPFL / Swiss Plasma Center · 2025–Present

Dr. Ahmed Hassanein
Plasma–Material Interactions
Purdue / Argonne · 2025–Present

Dr. Patrick E. Hopkins
Extreme Thermal Materials
U. of Virginia · 2025–Present

Dr. Peter Hosemann
Materials Joining & Structural Integrity
UC Berkeley · 2025–Present

Dr. Travis W. Knight
Advanced Nuclear Fuels & Systems
U. of South Carolina · 2025–Present

Dr. Philippe Lebrun
Cryogenics & Magnet Cooling
CERN · 2025–Present

Dr. Nitendra Singh
Nuclear Safety & Fuel Cycle
ITER · 2025–Present

Dr. Guido Van Oost
Magnetic Confinement & Fusion Systems
Ghent University · 2025–Present

Dr. Gary S. Was
Radiation Materials & Structural Integrity
U. of Michigan · 2025–Present

Dr. Ray Sedwick
Direct Energy Conversion
U. of Maryland · 2025

OPERATIONS

Michael Laughlin
Chief Operating Officer
2022–Present

Martin Owens
Chief Strategy Officer
LANL / GE Hitachi · 2022–Present

MG (Ret.) Paul Pardew
Chief Contracting Officer
Army Contracting Command · 2022–Present

David Beck
Fusion Commercialization
U.S. Space Force · 2024–Present

Sushma Bhatia
Environmental & Legislative
Google · 2022–Present

Michael De Frenza
Technology Licensing
2023–Present

MG (Ret.) Robin L. Fontes
Cybersecurity & Defense
Army Cyber Command · 2022–Present

Vijay Gehani
Supply Chain & Components
INOX India · 2024–Present

Jon Michel Greenwood
IT & AI Infrastructure
Live Nation · 2023–Present

Brian C. O'Neill
National Security
CIA / ODNI · 2022–Present

Gen. (Ret.) Gustave F. Perna
DoD Liaison
Operation Warp Speed · 2022–2023

Andrea Romero
Marketing Lead
2022–Present

Legal counsel is retained; those roles are held on the internal roster and are not listed here.

SOURCES

References

1 R F Post, Mirror systems: fuel cycles, loss reduction and energy recovery, in *Nuclear Fusion Reactors* (British Nuclear Energy Society, London, 1970) p. 99. doi:10.1680/nfr.44661.0007

2 R W Moir and W L Barr, “Venetian-blind” direct energy converter for fusion reactors, *Nucl. Fusion* **13** 35 (1973). doi:10.1088/0029-5515/13/1/005

3 W L Barr, R W Moir and G W Kinney, Experimental and computational results on direct energy conversion for mirror fusion reactors, *Nucl. Fusion* **17** 1015 (1977). doi:10.1088/0029-5515/17/5/012

4 W L Barr and R W Moir, Test results on plasma direct converters, *Nucl. Technol. – Fusion* **3** 98 (1983). doi:10.13182/fst83-a20820

5 R F Post, The magnetic mirror approach to fusion, *Nucl. Fusion* **27** 1579 (1987). doi:10.1088/0029-5515/27/10/001

6 T K Fowler, R W Moir and T C Simonen, A new simpler way to obtain high fusion power gain in tandem mirrors, *Nucl. Fusion* **57** 056014 (2017). doi:10.1088/1741-4326/aa5e54

7 V P Pastukhov, Collisional losses of electrons from an adiabatic trap in a plasma with a positive potential, *Nucl. Fusion* **14** 3 (1974). doi:10.1088/0029-5515/14/1/001

8 D E Baldwin, End-loss processes from mirror machines, *Rev. Mod. Phys.* **49** 317 (1977). doi:10.1103/RevModPhys.49.317

9 N Noda and Y Yasaka, Simulation experiment on traveling-wave direct energy converter, *Fusion Technol.* **33** 71 (1998). doi:10.13182/fst98-a32

10 Y Yasaka *et al*, Experimental simulation on direct energy converter for D–^{3}He fusion using RF traveling wave, *AIP Conf. Proc.* **595** 138 (2001). doi:10.1063/1.1424247

11 T Nakamoto, Enhanced energy recovery in a secondary electron direct energy converter through reduction of the magnetic mirror effect, *Fusion Sci. Technol.* **68** 341 (2015). doi:10.13182/fst13-900

12 G L Kulcinski and J F Santarius, New opportunities for fusion in the 21st century – advanced fuels, *Fusion Technol.* **39** 480 (2001). doi:10.13182/fst01-a11963282

13 J F Santarius, G L Kulcinski, L A El-Guebaly and H Y Khater, Could advanced fusion fuels be used with today's technology?, *J. Fusion Energy* **17** 33 (1998). doi:10.1023/A:1022565231919

14 H-S Bosch and G M Hale, Improved formulas for fusion cross-sections and thermal reactivities, *Nucl. Fusion* **32** 611 (1992). doi:10.1088/0029-5515/32/4/I07

15 S Dushman, Thermionic emission, *Rev. Mod. Phys.* **2** 381 (1930). doi:10.1103/RevModPhys.2.381

16 D Endrizzi *et al*, Physics basis for the Wisconsin HTS Axisymmetric Mirror (WHAM), *J. Plasma Phys.* **89** 975890501 (2023). doi:10.1017/S0022377823000806

17 J E Menard *et al*, Fusion nuclear science facilities and pilot plants based on the spherical tokamak, *Nucl. Fusion* **56** 106023 (2016). doi:10.1088/0029-5515/56/10/106023

18 B N Sorbom *et al*, ARC: a compact, high-field, fusion nuclear science facility and demonstration power plant with demountable magnets, *Fusion Eng. Des.* **100** 378 (2015). doi:10.1016/j.fusengdes.2015.07.008

19 A J Creely *et al*, Overview of the SPARC tokamak, *J. Plasma Phys.* **86** 865860502 (2020). doi:10.1017/S0022377820001257

20 L Fedeli *et al*, Pushing the frontier in the design of laser-based electron accelerators with mesh-refined particle-in-cell simulations on exascale-class supercomputers (WarpX), *Proc. SC22*, IEEE (2022). doi:10.1109/SC41404.2022.00008

21 J Derouillat *et al*, SMILEI: a collaborative, open-source, multi-purpose particle-in-cell code for plasma simulation, *Comput. Phys. Commun.* **222** 351 (2018). doi:10.1016/j.cpc.2017.09.024

22 P K Romano *et al*, OpenMC: a state-of-the-art Monte Carlo code for research and development, *Ann. Nucl. Energy* **82** 90 (2015). doi:10.1016/j.anucene.2014.07.048

23 P Giannozzi *et al*, QUANTUM ESPRESSO: a modular and open-source software project for quantum simulations of materials, *J. Phys.: Condens. Matter* **21** 395502 (2009). doi:10.1088/0953-8984/21/39/395502

COLOPHON

How this document was made

The Kronos Fleet — Combined Editorial, 2026 is set in **Fraunces** (display), **Gelasio** (text), and **IBM Plex Mono** (data & equations), carried forward from the Kronos editorial design system.

The figures are rendered at 300 dpi from the deposited generator scripts; the document is composed as a single self-contained file with embedded fonts and imagery, paginated to US Letter, and rendered to PDF through a headless Chromium engine in matched light and dark editions.

Every headline quantity carries an evidence class; withdrawn and restated values are marked as such. Nothing herein is frozen beyond the founder-approved Tier-A set.

Explore it live — turn the interactive 3-D model, run the deposited solvers in the physics validator, and watch the companion film series.

LEGAL NOTICE

Notice, status, and distribution

Conceptual design & simulation study. This document reports a conceptual design and simulation study. It is not a construction commitment, a safety-analysis report, a regulatory filing, or an offer of securities. Forward-looking statements — schedules, costs, market sizes, and performance — are estimates subject to the limitations set out in the Simulations part and may change.

Numbers and their classes. Quantities are reported with evidence classes and case labels; modelled, assumed, and requirement-class values are identified as such and are not to be quoted without their labels.

Public edition. This edition carries the physics and design only; all financial, funding, and defense-commercial content has been removed for public distribution. The scientific text corresponds to the arXiv and journal submissions.

THE 2026 KRONOS SERIES

One programme, many papers

This editorial is one paper in the Kronos 2026 series — a real fusion company's complete, reproducible physics record for a spherical-tokamak breeder and its low-neutron D–^{3}He tandem-mirror burners. Every headline number is a frozen anchor in the Physics De-Risking Register.

Explore the whole programme: the De-Risking Register, the interactive 3-D model, and the physics validator.

KRONOS FUSION ENERGY

Direct-Energy-Converter Architectures for a D–^{3}He Tandem-Mirror Burner: Venetian-Blind, Traveling-Wave, and Periodic-Electrostatic-Plug Collectors Compared on Efficiency, Grid Erosion, and Lifetime

A real fusion company building real machines. Explore the science, live.

Zenodo · doi:10.5281/zenodo.22645935

Read on kronosfusionenergy.com

The Physics De-Risking Register